Next Generation Photonic True Time Delay Devices as Enabled by a New Electro-Optic Architecture

Scott R. Davis,* Seth T. Johnson, Scott D. Rommel, and Michael H. Anderson
Vescent Photonics Inc., 4865 E. 41st Ave., Denver CO 80216

ABSTRACT

We present new photonic-true-time-delay (PTTD) devices, which are a key component for phased array antenna (PAA) and phased array radar (PAR) systems. These new devices, which are highly manufacturable, provide the previously unattainable combination of *large time delay tunability* and *low insertion loss*, in a form factor that enables integration of many channels in a compact package with very modest power consumption. The low size, weight, and power are especially advantageous for satellite deployment. These devices are enabled by: i) "Optical Path Reflectors" or OPRs that compresses a >20 foot change in optical path length, i.e., a >20 nsec tuning of delay, into a very compact package (only centimeters), and ii) electro-optic angle actuators that can be used to voltage tune or voltage select the optical time delay. We have designed and built OPRs that demonstrated: *large time delay tunability (>30 nsecs), high RF bandwidth (>40 GHz and likely much higher), high resolution (<200 psec)*, and *low and constant insertion loss (< 1 dB and varying by < 0.5 dB)*. We also completed a full design and manufacturing run of improved EO angle actuators that met the PTTD scanner requirements. Finally, a complete optical model of these integrated devices will be presented, specifically; the design for a multi-channel (400 channels) PTTD device will be discussed. The applicability and/or risks for space deployment will be discussed.

Keywords: optical time delay, true time delay, LC waveguides, liquid crystal, photonic time delay, phased array antenna, phased array radar, EO beamsteering

1. INTRODUCTION & OVERVIEW

We have designed and experimentally verified the feasibility of new optical time delay units (TDUs) or, as we refer to them, photonics true time delays (PTTDs). As will be shown these units can provide: i) large delay tunability of over 20 nsecs (35 nsec demonstrated), ii) high temporal resolution (~100 to 200 psec), iii) high carrier bandwidth (over 40 GHz demonstrated, but limit is certainly higher), iv) no-moving parts, rugged, electro-optic (EO) control, v) high and constant optical throughput (>90%, varying by less than 3% demonstrated), and finally, vi) highly integrable into multi-channel units in a small form factor. To our knowledge, these results represent improvements for delay tunability and throughput over previous approaches, all in a package that may be rugged and very low size, weight, and power (SWaP). Furthermore, the devices are constructed from materials that have a demonstrated high tolerance to radiation exposure, as may be required for space deployement.

The challenge of realizing both *low loss* and *large time delay tunability* (>15 nsec) for high bandwidth RF signals, in a cost effective and compact-multichannel package, has proven historically intractable. This is despite its importance in microwave signal processing,[1, 2] future optical communications networks,[3] and phased array antenna (PAA) and radar (PAR) systems.[4, 5] The landscape of prior approaches, represented in Figure 1, may be divided into either electronic or optical techniques. Within the optical domain there are two further sub-divisions, guided wave and free space. Guided wave techniques have the advantage of ruggedness but suffer from waveguide propagation and/or switch losses.[6-8] Free space approaches have the advantage of low propagation loss, but can be bulky and prone to misalignment.[9-11] Finally, all of the prior solutions have faced significant challenges with Size, Weight, and Power (SWaP) and/or cost.

* Corresponding author. Tel.: 303-296-6766; fax: 303-296-6783.
Email address: davis@vescentphotonics.com

Sensors and Systems for Space Applications VI, edited by Khanh D. Pham, Joseph L. Cox, Richard T. Howard, Genshe Chen, Proc. of SPIE Vol. 8739, 87390G · © 2013 SPIE · CCC code: 0277-786X/13/$18 · doi: 10.1117/12.2015302

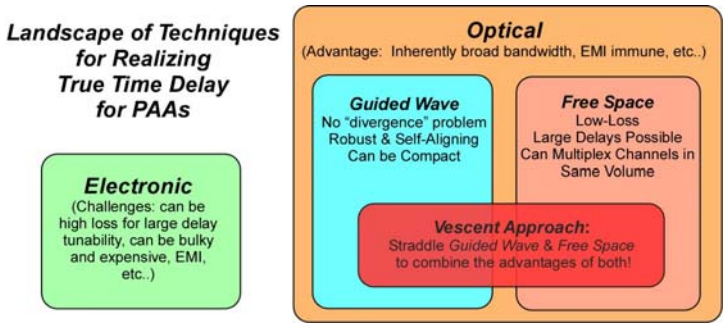

Figure 1: Overview of technical approaches that have been explored to realize time-delay tunability.

Our architecture combines the inherent low-loss of free-space optics *with* the ruggedness and compactness of guided wave optics. Importantly, this approach realizes *large time delay tunability* and *low insertion loss*, all in a form factor that enables integration of many channels in a compact, rugged, and economic package. A schematic depiction of a photonic-true-time-delay (PTTD) system that utilizes this architecture, with hundreds or even 1000 independent channels, is shown in the top of Figure 2. We refer to this integrated PTTD device as a "window-pane", due to the slim (~1 cm thick) form factor.

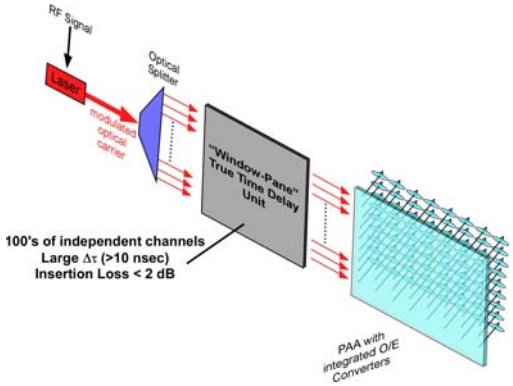

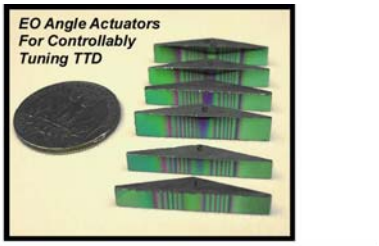

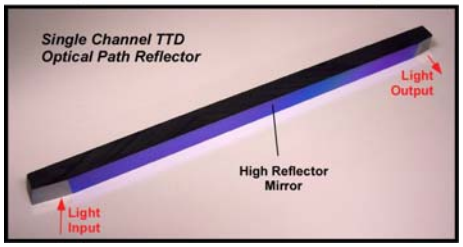

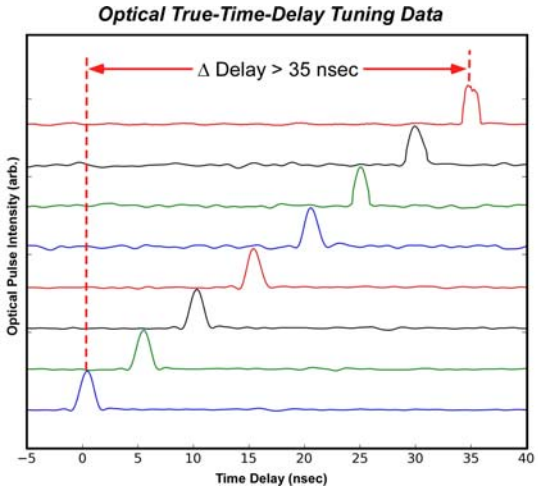

Figure 2: Top) Schematic of the "Window-Pane" photonic true time delay. Lower Left) Pictures of both micro-EO angle actuators for controllably altering the time delay and an OPR prototype for compressing the large change in optical path length into a compact package. Lower Right) Data showing optical pulses that have been controllably delayed over 35 nsecs.

To demonstrate feasibility of this approach three technical hurdles needed to be overcome. First, to realize large true-time-delay tunability (e.g. 20 nsecs) the optical path length must be changed or tuned a commensurately large amount (e.g. ~20 feet in air!). To establish that we could compress this large ~20 foot change into a very small package we needed to demonstrate unique "optical path reflectors" or OPRs. The lower left of Figure 2 shows a picture of a prototype "single channel" OPR that we designed and built. This OPR and others like it demonstrated a previously unattainable combination of true-time-delay performance characteristics: *large time delay tunability (>30 nsecs), high RF bandwidth (>40 GHz and likely much higher), high resolution (<200 psec)*, and *low and constant insertion loss (< 1 dB and varying by < 0.5 dB).* The lower right of Figure 2 shows optical pulses wherein their delay has been controllably tuned over a range of 35 nanoseconds. Second, a rugged and low-loss actuator that controllably alters the time delay was needed. To establish the feasibility of this we needed to improve and modify revolutionary electro-optic (EO) angle actuators.[12] As part of this effort we completed a full design and manufacturing run of improved EO angle actuators that met the scanner requirements (>10^o of out-of-plane, non-mechanical laser scanning) for PTTD devices. Pictures of example non-mechanical waveguide based EO actuators are shown in the lower left of Figure 2. Third, we needed to demonstrate that the EO angle actuators and the OPRs could be mated to form a photonic-true-time-delay (PTTD) device. We performed an optical-bench demonstration and realized ~10 nsecs of non-mechanical EO tuning over optical time delays. Finally, in the interest of exploring multi-channel integrated PTTD systems we developed an optical model of integrated PTTD devices. Table 1 shows the performance of possible devices with 256 independent optical delay lines. The total delay tunability is chosen by design (very large delays, e.g., >100 nsec, are possible); for this example we choose 20 nsec. The time-step resolution is also chosen by design; the table lists several example values ranging from 5-bit to 8-bit. The performance specifications (left column) will be discussed in the main body of this article.

Table 1: Some example designs for PTTD devices that are possible.

Specification	5 Bit	6 Bit	7 Bit	8 Bit	Notes
Delay Tunability[A]	20 nsec	20 nsec	20 nsec	20 nsec	
Time Step Resolution[A]	625 psec	313psec	156 psec	78 psec	
Insertion Loss	< .5 dB	< 1 dB	< 1.8 dB	< 3.0 dB	
Delay Dependent Change in Loss	< .3 dB	< .6 dB	< .6 dB	< 1.8 dB	Can be engineered to 0dB if desired
Time Step Reproducibility	180ppm/^{o}C	180ppm/^{o}C	180ppm/^{o}C	180ppm/^{o}C	Easily stabilized to 1ppm
Crosstalk	10^{-8} optical	10^{-8} optical	10^{-8} optical	10^{-8} optical	From beam overlap
RF Bandwidth[B]	> 40 GHz	> 40 GHz	> 40 GHz	> 40 GHz	
Power Consumption	< 50 μwatts per channel	< 50 μwatts per channel	< 50 μwatts per channel	< 50 μwatts per channel	
Mass	< 22 g per channel	< 16 g per channel	<31 g per channel	<10 g per channel	
Reconfigure Speed	500 μsec	500 μsec	500 μsec	500 μsec	
Ruggedness	No moving parts	No moving parts	No moving parts	No moving parts	
Channels	256	256	256	256	
Size	6×15×21cm	12×17×8.4cm	40×16×5.5cm	40×12×2cm	Some of these designs require multiple window-panes, which may be stacked.

[A] By choice of the OPR geometry one can readily trade off between total delay tuning range and resolution.

[B] The RF bandwidth of current devices is likely higher, potentially into THz. The 40 GHz number is listed because, through a related optical communications project, 40 GHz is what we have demonstrated.

In the remainder of this paper we will first describe the design, construction, and testing of the OPR. This enables compression of this change in optical path length. Second, we will briefly discuss the electro-optic (EO) angle actuators, by which the time delay may be tuned and we will present results on combining these two, thereby rendering a full EO PTTD demonstration. Finally, we will conclude with a brief discussion of multi-channel integrated devices.

2. THE OPTICAL PATH REFLECTOR: FOLDING "20 FEET" INTO CENTIMETERS

2.1. Review of the OPR concept: compressing a large change in path length into a small package

To realize time delay tunability over 20 nsecs, i.e., 20 feet, in a compact package we use a multi-pass optic to fold the path length into a much smaller package. While this folding to reduce the device size is not new, our approach has an important difference from prior efforts.[9, 10] Specifically, past efforts have used focusing elements to compensate for Gaussian beam spread. While including focusing elements seems intuitive (our initial designs included them), after considerable modeling we determined that the optimal geometry is simply two parallel reflectors, as shown in Figure 3. The angle at which the light is launched determines the total number of bounces and therefore the total transit time.

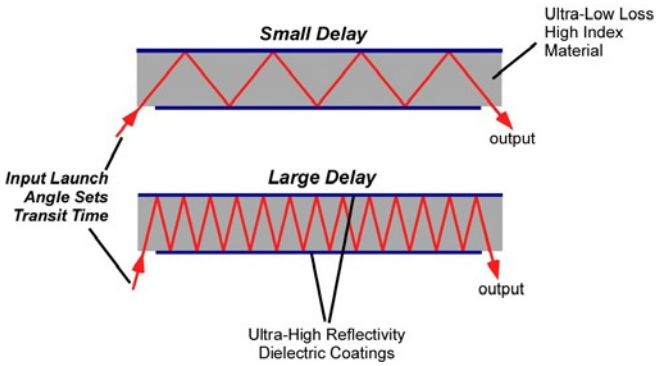

Figure 3: The basic concept of the "optical path reflector".

The OPRs are constructed from a solid slab of highly transparent silicon (Si), with mirrors coated directly onto the surfaces, thereby providing a rugged monolithic construction. The propagation inside the multipass region is a "free space" beam, which circumvents guided-wave scattering losses. Scattering losses were a key detriment of many earlier guided wave approaches. This surprisingly simple design combines the ruggedness of an integrated optic with the low insertion loss of a free space optic.

We have modeled this design, including beam spreading, optical re-coupling to SM fiber, losses, crosstalk, etc. Table 2 summarizes potential design concerns and their corresponding solution. These design issues are also discussed in the subsequent text.

Table 2: Potential problems and their design solution for the optical path reflector.

Potential Problem	Design Solution
Gaussian Beam Spreading Induced Losses	The launch beam size is increased until the spreading is minimal. In Si this works out to be a <2 mm wide beam for up to 20 nsec delays
Material Absorption Induced Losses	Use highly transparent single crystal Si:
Mirror Reflectivity Induced Losses	"6-nines" mirrors (R=99.9999%) are COTS technology contributing only 0.03% to the insertion loss.
Exit Spot Resolution: Crosstalk from the (N-1)th Bounce	To mitigate crosstalk on the Nth exit bounce from the (N-1)th bounce the length of the optical path reflector will be increased.
Maintaining Critical Alignment	Utilize active EO scanners to keep alignment locked, similar to telecom cross-connects.

The delay step size determines the height H of the reflector, as shown in Figure 4. Using the small angle approximation the delay time for one reflection is

$$\delta\tau \approx \frac{2H}{c/n}, \qquad \text{Eqn 1}$$

where n is the refractive index of the medium.

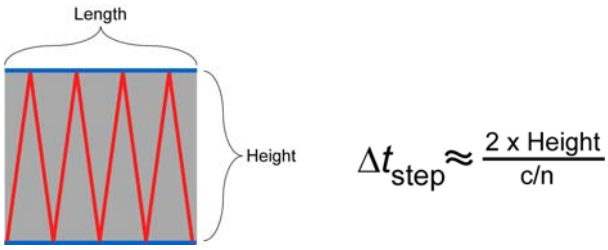

Figure 4: The height of the OPR is determined by the desired resolution. For a silicon OPR (n=3.5) to get a 200 ps resolution the height needs to be approximately 10 mm.

The magnitude of total time delay tunability desired determines the total number of bounces N through the relation $\Delta\tau = N\,\delta\tau$. This is schematically shown in Figure 5.

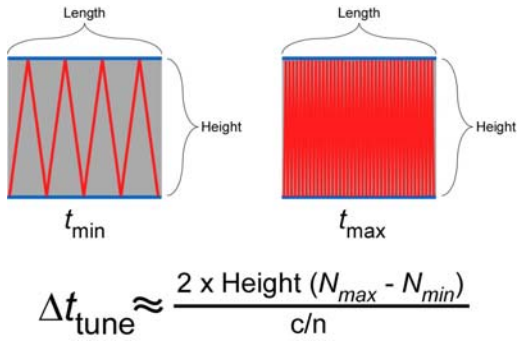

Figure 5: Once the height of the OPR is set, the total number of bounces is set by the desired total time delay. For example, with a 200 psec step size, to tune the TTD over 20 nsecs requires tuning over 100 bounces.

The delay $\Delta\tau$ determines the path length in the medium which we hold to twice the Raleigh length, which in turn defines the spot size radius ω_o (refereed to the input). The Raleigh length is related to the maximum time delay by

$$Z_R = \frac{\pi\omega_o^2 n}{\lambda} = \delta\tau N_{\max}\, c/n = (\Delta\tau + \tau_o)c/n \qquad \text{Eqn. 2}$$

where $\Delta\tau$ is the total tunable time delay, and τ_o is a delay offset that will be discussed later. Rearrangement gives $\Delta\tau \sim n^2$ and shows the benefit of a high index material. State differently, the diameter of the launch optical beam is chosen such that the longest path length through the OPR, i.e., the longest delay, is within two Rayleigh lengths. The relationship between an expanded beam waist and cross-talk is shown in Figure 6.

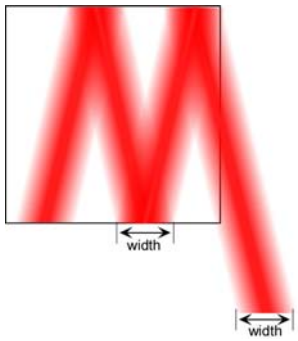

Figure 6: To mitigate the problem of Gaussian beam spreading the initial size of the optical beam is increased such that the maximum path length through the OPR (i.e., longest delay) is within two Rayleigh lengths.

Finally, the total length of the reflector is given by multiplying the spot diameter by the number of bounces

$$L = 2N_{\max}\alpha\omega_{o}, \qquad \text{Eqn. 3}$$

The parameter α is determined so that the spot spacing at the exit will be sufficiently large to prevent light from the N_{max}-1 bounce from spilling onto the exit aperture, and it accounts for beam spreading in the OPR. In all of our designs we chose the cross-talk at less than one part per thousand. A new design decreases the cross talk to less than one part per 10^8. The crosstalk may be reduced by lengthening the OPR as is schematically shown in Figure 7. This drives the aspect ratio of the OPR to be long and skinny. While it seems obvious now this was an important realization.

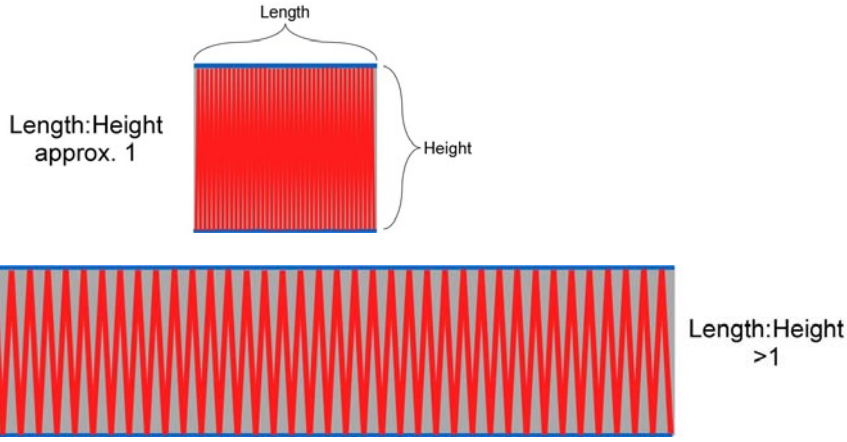

Figure 7: To mitigate cross-talk between the N^{th} bounce and the $(N-1)^{th}$ bounce the aspect ratio of the OPR may be stretched. The advantages to a long and skinny form factor are significant, as discussed in the text and in the results section.

Starting from a high number of bounces also reduces the beamsteering or angle actuator requirements. The meaningful figure of merit for a beamsteerer is how many resolved spots it creates in the far field. (The number of resolved spots is the total steering range divided by the spreading angle of the Gaussian beam). Another important realization for useful operation of OPR devices is that the total number of bounces through the device should start at a large value, such that the small angle approximation w.r.t. the OPR mirror is valid. This ensures that the TTD step size is constant with changing delay. This is shown in Figure 8.

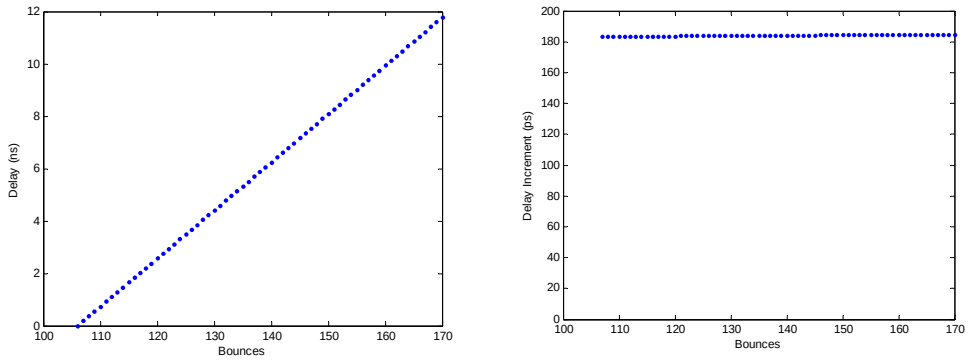

Figure 8: Left) The theoretical TTD of an OPR as a function of number of bounces. Right) Example change in TTD, i.e., step size as a function of number of bounces.

2.2. The real word design requirements for useful OPR devices.

While the simple OPR concept looks great on paper (a critical requirement!) the task of building demonstrator devices necessitates several performance requirements. These include:

1) We need highly transparent silicon. The path length inside the OPR can exceed two meters. For devices with greater than 80% optical throughput this requires an absorption coefficient of less than 10^{-3} cm^{-1}. As will be shown, we have exceeded this by more than an order of magnitude.

2) We need very good mirrors. All of our OPR designs have the total number of bounces inside the device as ranging from nearly up to 100 to over 200 reflections. This necessitates a reflectivity of >99.99%. This is a so-called "4-nines" mirror. "6-nines" mirrors are standard COTs coatings.

3) The silicon needs to have high parallelism. Deviations in parallelism, specified as a total thickness variations (TTV) but be less than 2 microns, otherwise the optical beam will walk or be directed "off course".

4) The silicon surfaces must be of high quality. Since the optical beam will be bouncing off the surface over 100 times any scratches or digs could be problematic.

During this effort we have met and/or exceeded all of these requirements.

2.3. OPR Experimental Results

The first task was to find high purity, high transparency, and thick silicon. We procured thick silicon candidate materials from five different foundries. All of the test silicon materials, from all of the vendors, were measured for transparency. The summary of these results is plotted in Figure 9 and presented in Table 3. Somewhat to our surprise the task of realizing sufficient silicon transparency was more difficult than anticipated. Our unjustified early confidence was based on previously published experimental absorption coefficients, which are plotted in Figure 9 as blue circles. [13-15] These prior data points show a very monotonic and expected relationship between resistivity and optical absorption over many decades of variance in each. This monotonic relationship is expected based on absorption that is dominated by free-carrier effects. [15]

Table 3: Summary of the silicon that we have procured for this project, along with the absorption implications for a 10 nsec (160 cm path length) TTD device.

Type of Growth	Doping	Resistivity (Ohm-cm)	Absorption Coefficient (1/cm)	Optical Throughput for 10 nsec TTD
CZ	P-doped	82 ± 50	3.4×10^{-3}	58%
CZ	Intrinsic	180 ± 100	1.9×10^{-2}	5%
CZ	Intrinsic	540 ± 217	3.3×10^{-2}	0.5%
CZ	Intrinisc	750 ± 550	1.9×10^{-2}	5%
CZ	P-doped	50 ± 30	4.8×10^{-3}	46%
MCZ	**Intrinsic**	**>1000**	**$<1.0 \times 10^{-4}$**	**>97%**
FZ	Intrinsic	500-5000	2.0×10^{-2}	5%
FZ	Intrinsic	>1000	5.5×10^{-3}	40%
FZ	**Intrinsic**	**>1000**	**$<2.0 \times 10^{-4}$**	**>93%**

Most silicon is usually grown doped, which impacts the resistivity and therefore the IR transparency via free carrier absorption. Since our design requires silicon path lengths of several meters we are especially sensitive to any absorption. We therefore needed to both understand the dopant / absorption relationship and to procure silicon with an appropriately small dopant level. We calculated the silicon absorption levels as a function of resistivity, as shown in Table 4, along with the expected OPR throughput assuming a pathlength of 2 meters. To do this calculation we made the assumption that the absorption coefficient has a linear dependence on the doping level. This is validated by the experimental data from Refs [13-15]. Based on this,

Table 4. Theoretically expected transmission characteristics for various levels of resistivity based solely on free-carried induced absorption.

Resistivity (Ω cm)	Free-Carrier Predicted Absorption Coefficient (cm^{-1})	I/I_0 (%)
10	0.010560	5.66
20	0.005240	24.04
80	0.001304	70.14
1000 (close to intrinsic)	0.000104	97.21

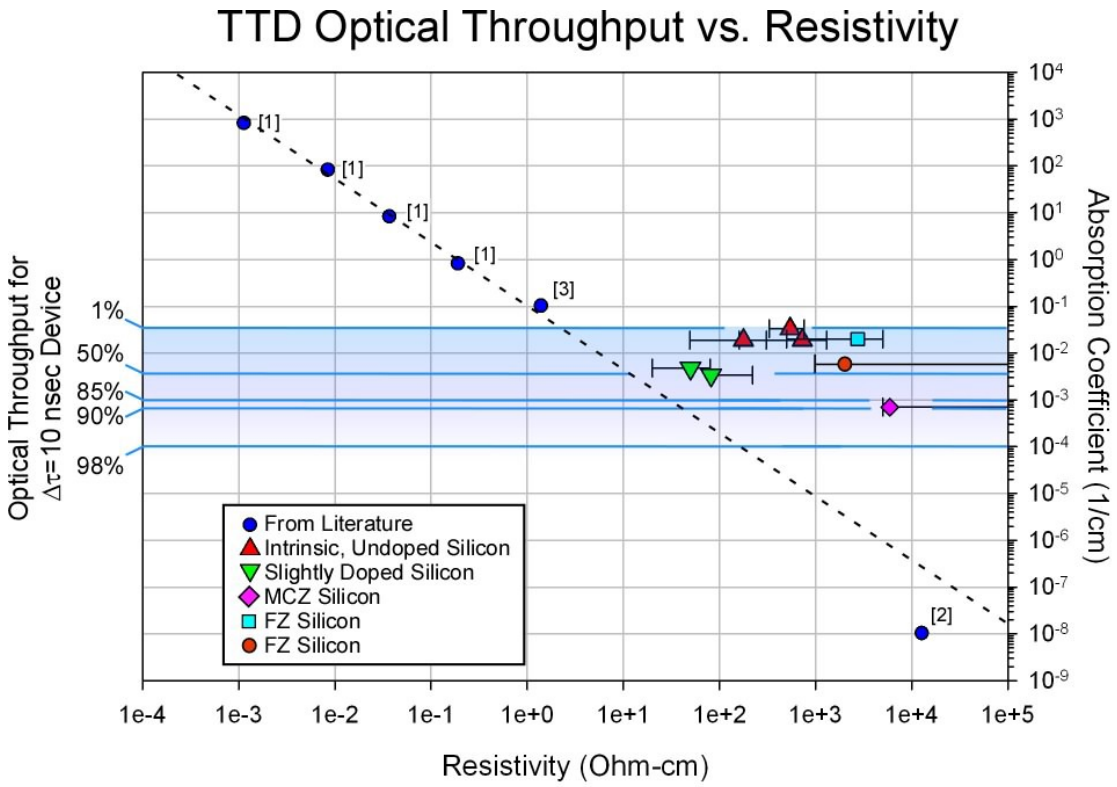

[1] Falk, R.A., *Near IR absorption in heavily-doped silicon: An empirical approach*, (ISTFA) International Symposium for Testing and Failure Analysis, 2000
[2] Keevers, M.J. and Green, M.A., *Extended infrared response of silicon solar cells and the impurity photovoltaic effect*, Solar Energy Materials and Solar Cells, Volumes 41-42, Pages 195-204, June 1996.
[3] Spitzer, W. and Fan, H. Y., *Infrared Absorption in n-Type Silicon*, Phys. Rev. 108, Issue 2, 268–271, 1957.

Figure 9: Plot of measured 1550 nm absorption coefficients (right axis) as a function of silicon resistivity. This plot contains data from all of the Float Zone, Intrinsic, doped CZ, and MCZ material that were considered as candidate OPR silicon. The blue circles are experimental values taken from the literature. All other data points are our experimental values. All of the silicon is more absorptive than one would expect from the resistivity (approximated by the dashed black line). It is interesting to note that below an absorption coefficient of approximately 0.1 then non-dopant contaminants (e.g. oxygen) dominate absorption effects. Nevertheless, since we are below the 10^{-3} level (our performance criteria) with MCZ (pink diamond and orange pentagon) and FZ (yellow square) we have several suitable sources of low absorption silicon.

For all of the data taken during this project, plotted as colored symbols in Figure 9, the measured absorption deviates from a simple free-carrier or resistivity dependence. The absorptions are significantly larger than a simple free-carrier effect would predict, in some cases several orders of magnitude larger. We have identified contaminant oxygen, which causes "mid-band" multi-photon induced absorption, as a likely source. The MCZ silicon, with a low oxygen content, provides the best optical transparency. The FZ silicon also has excellent transparency. The absorption coefficient for the MCZ was $<1.0 \times 10^{-4}$ cm^{-1}, which will provide TTD devices with 10 nsec of tunability and nearly 98% optical throughput.

To turn the transparent silicon into an OPR we first needed to apply the HR mirrors. A dielectric stack was designed to provide a 99.99% (four-nines) mirror. This was applied to both sides via an ion beam sputter process.

The optical bench set-up for testing the first OPR devices is shown in Figure 10. We utilized a high speed pulser (from Avtech) that generates fast rise time pulses (<0.1 ns) that are 2 nsec long and designed for driving a 50 ohm load such as a lithium-niobate eletro-optic modulator. The EOM was manufactured by EO-space and has a 12 GHz bandwidth. This was used to create short pulses of light which were coupled into the OPR device. Specifically, the output of the EOM is fiberdized. We attached this to a GRIN lens with a 1 mm collimated, low M^2 output. This output was directed into the OPR. The OPR was mounted to a precision rotation stage (0.001 degree resolution), with the input point of the OPR set

to the center of the rotation stage. By rotating the stage one may therefore tune the number of bounces realized through the OPR, and therefore tune the time delay. The output light was collected on a high speed photodetector (10 GHz) from Electro-Optic Technologies (EOT). This was used to record the light pulses after traveling through the OPR test device. A high speed digital scope, which is also triggered from the Avtech pulser, was used to measure the delay. The detector was mounted onto the same rotation stage as the OPR so it maintained alignment.

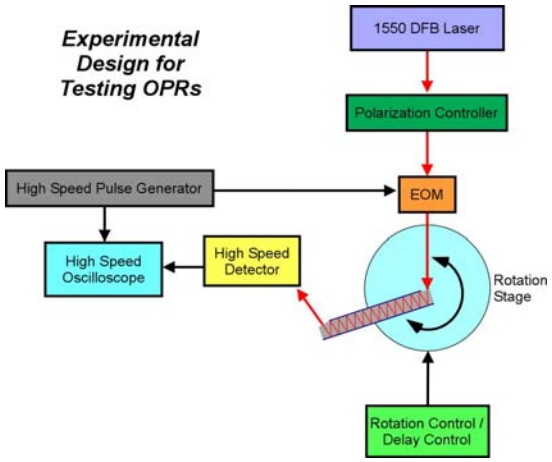

Figure 10: Schematic of the experimental test-bed for assessing the OPRs.

Figure 11 shows a picture of the device as the light is "rattling" around between the two mirrors one a first generation OPR device. Since the beam is in the IR at 1550 nm, this was recorded with an InGaAs CCD camera. Each spot or mirror reflection is clearly visible (this is the 0.01% of light that is transmitted through the 99.99% mirror). As the launch angle into the OPR is changed (in this example by mechanically rotating the OPR, though ultimately this will be done with our EO angle actuator) the number of bounces, and therefore transit time through the device, is varied. In Figure 11 three frames from a movie are shown wherein the number of bounces is controllably changed from a smaller value (top) to a larger value (bottom). The spots on the top are brighter because at this incidence angle the IBS mirrors are less reflective, i.e., they let more light through.

An example of optical pulses transmitted through an example OPR that can be controllably delayed is shown in Figure 1. In this example the delay of an optical pulse "rattling" through an OPR could be controllably tuned over 35 nsecs. This OPR device had a temporal-delay step size or resolution of 380 psecs.

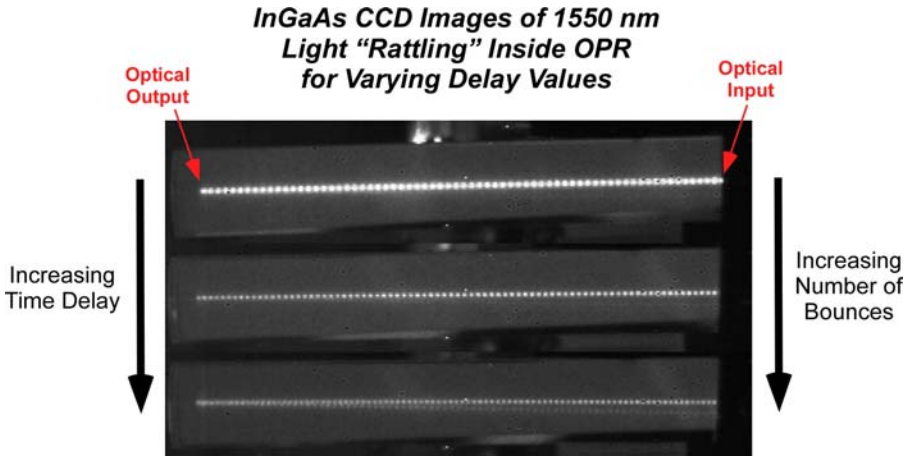

Figure 11: Picture of a 1550 nm optical beam as it "rattles" through a second generation OPR device. The Fresnel reflection off the exit silicon facet can be seen in the bottom figure, as it rattles back through the OPR.

To measure the optical throughput of the OPR we placed an optical power meter before and after the OPR. This allowed us to directly measure the optical throughput of the device as the TTD was scanned. We also corrected for the Fresnel losses at the silicon input and output surfaces, since this would not be present in the full device. The total optical throughput as a function of time delay for an example OPR devices is plotted in Figure 12. The sharp cut-off in throughput at the low delay end is due to the dielectric stack mirror hitting its design edge. The decrease in throughput with increasing delay is entirely explained by a 99.99% mirror reflectivity (red-line in plot). By simply ordering an "extra 9" (6-nines mirrors are COTs) we expect to have extremely transparent (<3%) OPRs!

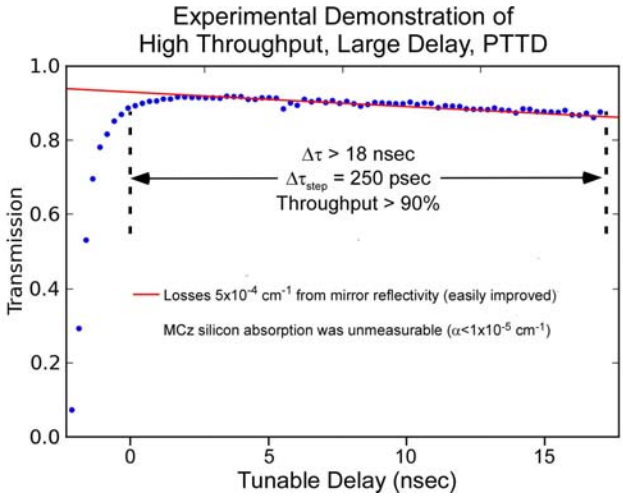

Figure 12: Example performance from a second generation OPR device. The optical losses were determined to be from the mirrors. A tweak of the mirror designs will greatly minimize this. The silicon absorption for this MCZ material was below our measurement limit; it is effectively completely transparent.

Finally, we also acquired images of the beam quality after it has bounced through the OPR. The beams coming out of the OPRs should be essentially perfect replicas of the input beams. Examples are shown in Figure 13; these are nearly indistinguishable from light emerging from a single mode optical fiber.

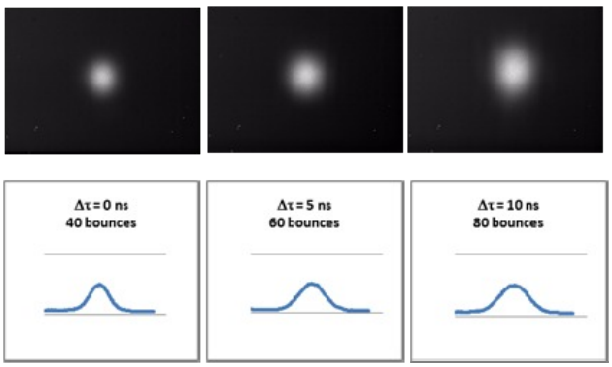

Figure 13: Example images of the output optical beam after it has bounced through one of the OPRs. These are essentially perfect beams, comparable to emission from a single mode fiber.

3. EO ANGLE ACTUATORS FOR CONTROLLABLY ALTERING THE TIME DELAY

In order to controllably alter the time delay one must tune both the "launch" and "receive" angles at which the light enters and exits the OPR. This requires an optical angle actuator. These can be realized with mechanics, but mechanics are power consumptive, have wear issues, are prone to vibrations, and can be bulky. A non-mechanical or EO scanner is therefore desired. Unfortunately, despite both the tremendous desire and the significant amount of resources and time expended viable EO alternatives to mechanics are still not available. Past attempts (e.g., DARPA-STAB, APPLE, etc.)

have yielded wide-angle, discrete-step birefringent prisms,[16-18] but these are bulky, expensive, slow, and have wide gaps between scan angles. To fill in the gaps between the discrete angles (> 90% of FOV not addressed), past approaches have utilized tunable diffraction gratings, such as LC optical phased arrays (OPAs),[19-21] MEMs arrays,[22, 23] electro-wetting arrays,[24] and acousto-optics. Despite significant advances (e.g., the Boulder Nonlinear 12,000 element array[25]), inherent limitations remain. For example, step scanning in OPAs depends on LC relaxation times (5 to 30 ms[25]), so a 500 point scan would take several seconds or even minutes! Furthermore, OPAs scan in discrete step-wise 2π resets and, therefore, suffer "blind spots" in the FOV into which they cannot steer. While diffractive fine-steering elements have fundamental problems, prior *refractive* scanning attempts have realized only small scan angles and/or large beam divergence.[26-31] Until now, this has been a problem without a solution.

Rather than continue down the very well trodden "diffractive-path" we have taken a unique approach to this historically intractable problem. We exploit the giant electro-optic phase control (voltage tuning of optical phase by > 2 mm) provided by of our proprietary liquid-crystal (LC) clad optical waveguides[32-34] to construct unparalleled *refractive* EO scanners. For near-IR operation (λ~1.5 μm) we have recently demonstrated: i) a 1-D beamsteerer with a remarkable steering range of >80° even making light loop upon itself in certain geometries (270°), ii) wide-angle continuous coverage 2-D beamsteerer (50°× 15° per chip) , iii) high speed scanning (60 kHz demonstrated), and iv) a large aperture scanner (1.2 cm demonstrated). Figure 14 shows EO scanners which may be extremely compact (~2cm^3). They are also inherently low power consumption (only milliWatts) and very simple (only 3-control electrodes for 2-D steering). Finally, the elegance of the design allows for very low cost volume production, ultimately similar to the ubiquitous LC-display.

The enabling innovation is to utilize liquid crystals (LCs), which have by far the largest electro-optic response of any known material (R_{33} ~ 10^6 pm/volt compared to ~20 pm/volt for $LiNbO_3$), in a new geometric configuration that circumvents their historic limitation. Rather than transmit through an LC cell, which by design must be thin (typically < 20 μm), we use the LC as an active cladding layer in a waveguide architecture in which the light is confined to a high index core and the evanescent field extends into the variable-index liquid-crystal cladding (see right of Figure 14). Because the light is confined to the region near the surface where the LC molecules are strongly coupled, they experience strong restoring forces leading to dramatically lower scattering and very fast response times (<500 μsecs). Furthermore, by placing the LC in the evanescent field of the guided optical wave the interaction length is completely decoupled from the thickness of the LC layer, i.e., *large interaction lengths (up to cm's) are possible with a nicely behaved thin (~5 μm) LC-layer*. This not only circumvents limitations of traditional LC-optics, but it also surpasses the optical phase control performance capabilities of any other EO or MEMs optical system (voltage control over millimeters of optical phase are realized).

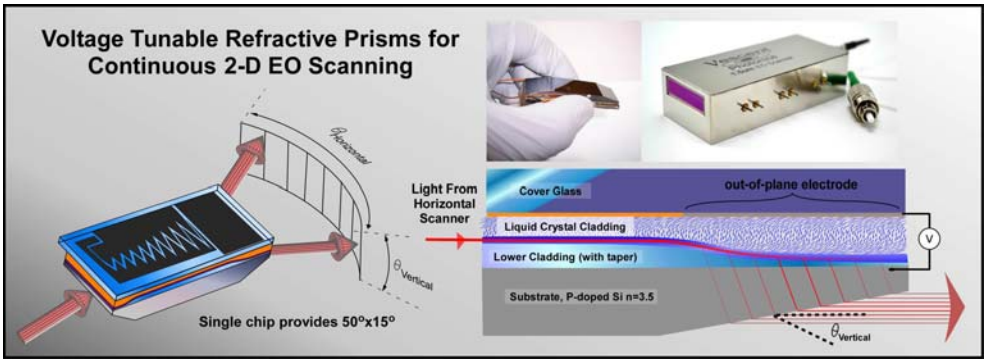

Figure 14: New wide angle, continuous, refractive EO beamsteerers as recently demonstrated by Vescent Photonics. The light is steered via a voltage tunable Snell's law refraction, either with prism electrodes (horizontal) and/or an out-coupling prism (vertical). The light input and output is a collimated beam. The upper right shows pictures of recent devices.

Unprecedented voltage control over optical phase enables unprecedented refractive scanning. Horizontal beam steering is achieved by prism shaped electrodes whose index may be voltage tuned (left of Figure 14). Vertical beam steering is achieved by allowing the evanescent field to tunnel into the high-index silicon substrate by tapering the subcladding

(right of Figure 14). An S-taper provides a Gaussian output with M^2~1. The output angle $\theta_{vertical}$ may be voltage tuned. This provides 2-D tunable refraction with a $50^o \times 15^o$ FOV and a <2mrad divergent beam. Figure 15 shows both scan angle data (left) and superimposed frames from a IR-CCD acquired movie wherein a 1550 nm beam was scanned across a parking lot (right).

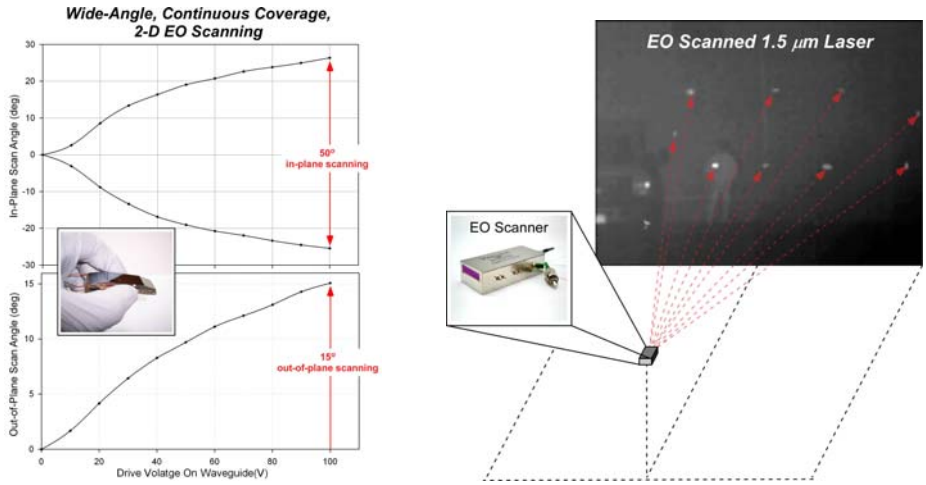

Figure 15: LEFT) Plot of measured EO scan angle as a function of waveguide voltage. The inset picture shows an EO scan waveguide. RIGHT) Superimposed frames from a movie (recorded with an IR InGaAs CCD) showing EO scanning of a 1550 nm laser across a parking lot.

In addition to the inherent rugged construction and elimination of all moving parts the LC-waveguide devices are built from materials with demonstrated radiation hardness[35] (> 45 Mrad of Gamma[36] and > 2 Mrad of electron[37]).

Ultimately, the EO angle actuators will be either optically contacted or grown directly onto the inputs, and possibly the outputs, of the OPR. To help establish feasibility we performed an optical bench mockup of an integrated system and a complete optical model of a fully integrated device. We assembled a benchtop station for testing an integrated EO TTD device. At the beamsteerer output is an optical arrangement that creates a virtual image of the beam pivot, which is actually located inside the beamsteerer. We want the EO angle actuator pivot to be located exactly at the OPR entrance window. While this is not a full integration we effectively used a telescope to "optically" place the EO scanner onto the surface of the OPR. At the output of the OPR a lens was used to image the exit spot either directly onto a high speed photodiode or into a large mode field diameter multi-mode fiber. Since the fiber length was short we did not worry about optical dispersion for these time studies. The optical pulsing and timing electronics were the same as with the setup used to test TTD on the OPR devices described earlier. With this setup we were able to demonstrate EO tuning of a pulses optical delay by nearly 10 nsecs.

3.1. Putting It All Together: A Fully Integrated Photonic True Time Delay

A benefit of the EO angle actuator is that it can steer out of the waveguide enabling fabrication directly onto the OPR. Furthermore, the beam has a near perfect fulcrum about the exit, which minimizes beam walk during tuning. Figure 16 shows how the waveguide based EO angle actuator can be used to control the number of reflections inside the OPR. A

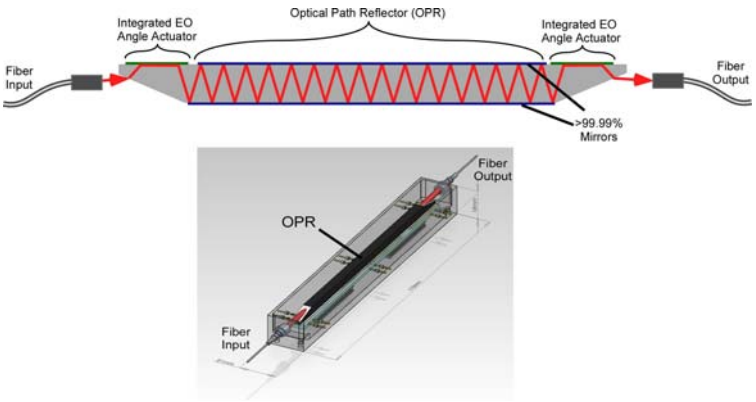

Figure 16: Example of a packaged, single channel OPR.

passive coupler couples light into a waveguide section adjacent to the OPR and a second tunable actuator couples the light into the OPR. An example of a single channel, packaged TDU is shown in the bottom of Figure 16. On the other side of the OPR a second pair of waveguide couplers operates in reverse to couple the light out to an optical fiber.

By extending the OPR in the other dimension to form a "window pane" then hundreds of PTTDs can be integrated into a single unit with the result that the device size per actuator becomes very small when compared to other approaches – on the order of 20 grams of silicon per TTD channel. Figure 17 shows a solid model of an integrated device wherein 200 light beams enter along two edges for a total of 400 TTDs. Couplers are optically contacted to the edge of the windowpane OPR. In addition, a frame-like assembly of fibers and GRIN lens collimators would be affixed over the top of the device providing the input and output fibers. Each fiber collimator would be aligned and fixed to the input/output Ulrich coupler using techniques common to the telecom industry. In many ways the packaging steps are similar to that used in large MEMS cross connect switches developed for telecom. The final device would house 400 independently addressed TTDs in an outer package about 1 foot on the side and perhaps 1-2 inches thick.

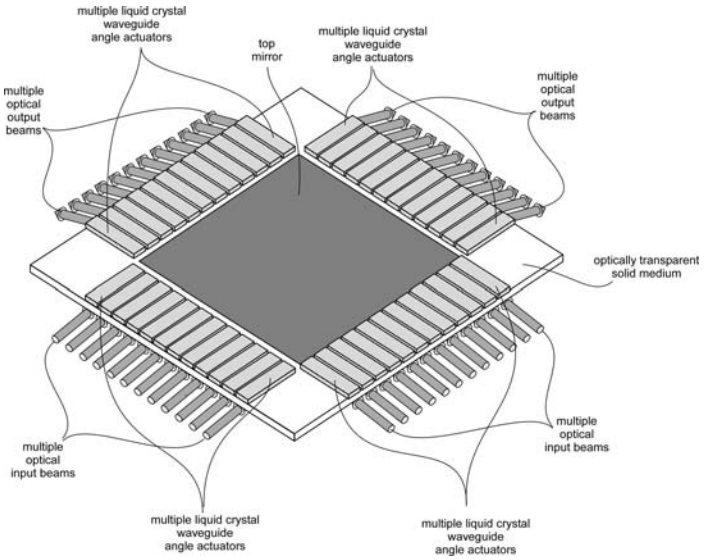

Figure 17. Solid model of the "window-pane" integrated true-time delay unit. For the rattle wedge design the inputs and outputs would be on the same side, but otherwise the form factor is similar.

4. CONCLUSIONS

We established the feasibility of new EO-PTTD devices through a series of experimental and numerical studies. Notably, we demonstrated unique OPR devices that provide very large time delay tunability (>20 nsec) with high optical throughput (>90%). We demonstrated improved EO angle actuators, which are required to voltage tune the delay. We

verified that these EO angle actuators meet the performance requirements for a PTTD device. Also, we demonstrated that these two elements can be mated together to form a full PTTD device. We have modeled multi-channel PTTD systems that we are confident we can build, with the specification listed in Table 1. The long-standing challenge is now one of engineering rather than invention and the decades old quest for optical true time delay devices is finally within reach.

5. ACKNOWLEDGMENTS

This work has been supported by the Missile Defense Agency through a phase I SBIR.